

## APPLYING DEEP LEARNING TO FAST RADIO BURST CLASSIFICATION

LIAM CONNOR<sup>1,2</sup> AND JOERI VAN LEEUWEN<sup>1,2</sup>

<sup>1</sup>*ASTRON, Netherlands Institute for Radio Astronomy, Postbus 2, 7990 AA Dwingeloo, The Netherlands*

<sup>2</sup>*Anton Pannekoek Institute for Astronomy, University of Amsterdam, Science Park 904, 1098 XH Amsterdam, The Netherlands*

### ABSTRACT

Upcoming Fast Radio Burst (FRB) surveys will search  $\sim 10^3$  beams on sky with very high duty cycle, generating large numbers of single-pulse candidates. The abundance of false positives presents an intractable problem if candidates are to be inspected by eye, making it a good application for artificial intelligence (AI). We apply deep learning to single pulse classification and develop a hierarchical framework for ranking events by their probability of being true astrophysical transients. We construct a tree-like deep neural network (DNN) that takes multiple or individual data products as input (e.g. dynamic spectra and multi-beam detection information) and trains on them simultaneously. We have built training and test sets using false-positive triggers from real telescopes, along with simulated FRBs, and single pulses from pulsars. Training of the DNN was independently done for two radio telescopes: the CHIME Pathfinder, and Apertif on Westerbork. High accuracy and recall can be achieved with a labelled training set of a few thousand events. Even with high triggering rates, classification can be done very quickly on Graphical Processing Units (GPUs). That speed is essential for selective voltage dumps or issuing real-time VOEvents. Next, we investigate whether dedispersion back-ends could be completely replaced by a real-time DNN classifier. It is shown that a single forward propagation through a moderate convolutional network could be faster than brute-force dedispersion; but the low signal-to-noise per pixel makes such a classifier sub-optimal for this problem. Real-time automated classification may prove useful for bright, unexpected signals, both now and in the era of radio astronomy when data volumes and the searchable parameter spaces further outgrow our ability to manually inspect the data, such as for SKA and ngVLA.

arXiv:1803.03084v1 [astro-ph.IM] 8 Mar 2018

## 1. INTRODUCTION

Fast radio bursts (FRBs) are bright, millisecond-duration, extragalactic radio transients, characterized by dispersion measures (DMs) that are significantly larger than the expected Milky Way contribution. They have been detected at flux densities between tens of micro Janskys to tens of Janskys (Lorimer et al. 2007; Thornton et al. 2013; Petroff et al. 2015; Ravi et al. 2016). The majority of early detections were made with the Parkes telescope multi-beam receiver, but in recent years detections have been made at Arecibo (Spitler et al. 2014), Green Bank Telescope (GBT) (Masui et al. 2015), the Upgraded Molonglo Synthesis Telescope (UTMOST) (Caleb et al. 2017), and the Australian Square Kilometre Array Pathfinder (ASKAP) (Bannister et al. 2017). FRB 121102 is the only source known to repeat (Spitler et al. 2016; Scholz et al. 2016), allowing for the first host galaxy localization using very long baseline interferometry (VLBI) (Marcote et al. 2017; Tendulkar et al. 2017). Recently, the repeating bursts from this source were found to be almost 100% linearly polarized with a Faraday rotation measure (RM) of  $10^5 \text{ rad m}^{-2}$  (Michilli et al. 2018).

There are likely thousands of detectable events each day across the full sky, but only  $\sim 50$  have been observed to-date. This is due to the moderate field of view (FoV) and relatively low duty cycle of current FRB surveys. Still, such surveys have produced thousands of false-positive triggers for each true FRB, the diagnostic plots of which have traditionally been inspected by eye (Masui et al. 2015; Amiri et al. 2017; Caleb et al. 2017; Foster et al. 2018). For upcoming fast transient surveys, the false-positive problem will be intractable if single-pulse candidates are to be human inspected, even with rigorous removal of radio frequency interference (RFI). The Canadian Hydrogen Intensity Mapping Experiment (CHIME) will search 1024 beams at all times, between 400–800 MHz and up to very high DMs (Ng et al. 2017). The Aperture Tile in Focus (Apertif) experiment on the Westerbork telescope will continuously search thousands of synthesized beams at 1.4 GHz (van Leeuwen 2014). ASKAP (Bannister et al. 2017) and UTMOST (Caleb et al. 2017) are also expected to have high detection rates, searching many beams with high duty-cycle. As a result, we will go from roughly five new FRB detections per year (2012–2017) to, potentially, thousands ( $> 2019$ ). This will also correspond with an orders-of-magnitude increase in the number of false positive candidates, meaning the generation of such events must be mitigated, and the process of sifting through them must be automated.

In pulsar searching, the problem is arguably worse due to the larger number of parameters involved, like period and its derivatives. Over the last decades, the ranking of pulsar candidates has involved an initial step of selection through simple heuristics, the main one being the peak signal to noise ratio of the profile over the noise. Thereafter, the astronomers go through the ordered list of candidate plots, looking for further pulsar signs such as broad-band, properly dispersed signal; a sharply peaked (not sinusoidal) folded profile; and steady emission throughout the observation. An experienced pulsar astronomer can average 1–2 plots per second, and human brains are very capable of singling out the most promising candidates. But modern multi-beam pulsar surveys, and the increasing bandwidths and new frequencies outside of radio-quiet protected spectrum are making this approach unfeasible. A telescope like LOFAR employs many hundreds of beams (van Leeuwen & Stappers 2010), and produces vast numbers of candidates. The LOFAR pilot surveys LPPS and LOTAAS (Coenen et al. 2014) produced  $\sim 20,000$  candidates, that were ranked and perused by humans. This took about four person-days. It found the first two pulsars with LOFAR. Shown in Fig. 1 is a subsection of the ranked list that included pulsar J0613+3731.

This approach is, however, reaching the limits of what is efficient. For a long-integration, multi-beam LOFAR search for young pulsars in supernova remnants, the lead author of Straal & van Leeuwen (2018) checked, by eye, the staggering number of 140,000 periodic candidates plus about 15,000 single-pulse candidates. This amounted to three full-time person weeks of time.

While efforts like the Pulsar Search Collaboratory (Rosen et al. 2013) have been successful in engaging hundreds of citizen scientists in ranking and analyzing candidates from GBT pulsar survey data, the overall person-power requirement remains unchanged and daunting.

The necessity of replacing manual inspection has led to a variety of approaches. Zhu et al. (2014) developed a sophisticated framework for pulsar candidate ranking, using multiple machine learning techniques to emulate a human expert inspecting diagnostic plots for tens of thousands of pulsar candidates from PALFA. They used convolutional neural networks (CNN) in tandem with support vector machines (SVM) on the pulsar candidates’ two-dimensional arrays, and ANNs with SVMs on one-dimensional data products, like pulse profile. Next, Guo et al. (2017) utilized a convolution generative adversarial network (DCGAN) to improve the ability of deep CNN classifiers.

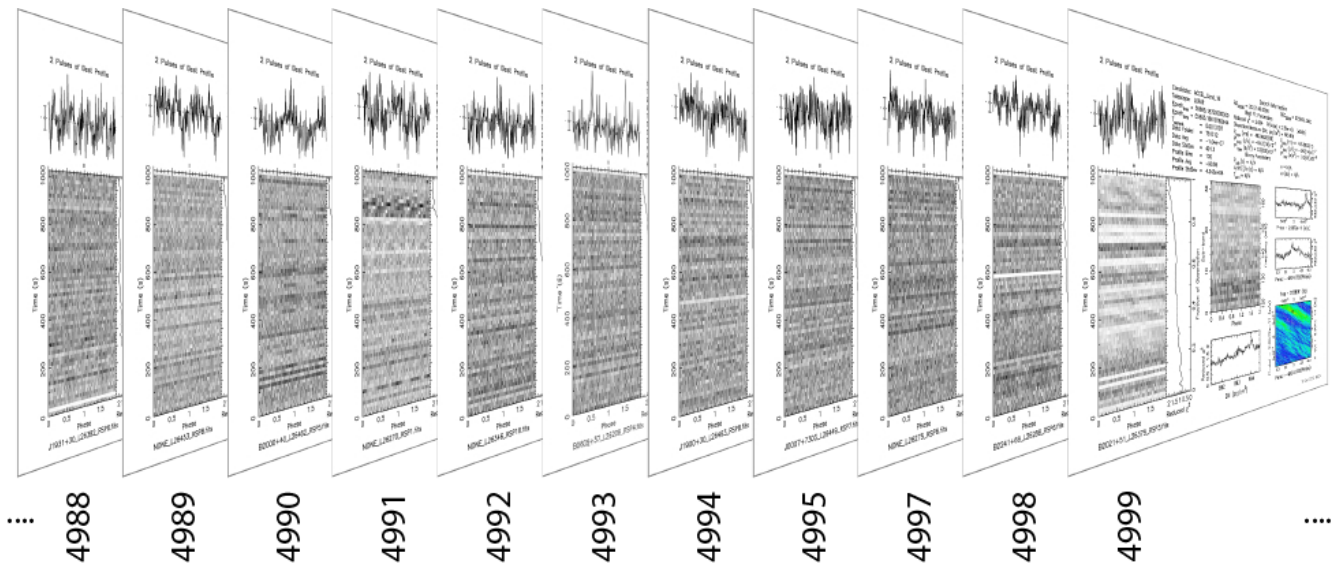


**Figure 1.** A small subset of the real-life diagnostic data used in the LOTAAS survey with LOFAR (Coenen et al. 2014). Out of  $\sim 20,000$  candidates, pulsar J0613+3731 was found by eye in plot #4993.

The LOFAR Tied-Array All-Sky Survey (LOTAAS) uses 222 digitally formed tied-array beams per pointing, and its search pipeline reports the  $\sim 100$  best periodic candidates per beam. Currently, in early 2018, 1500 pointings have been observed, and over 30 million periodic candidate signals were found. These can clearly no longer be inspected by eye. Thus Lyon et al. (2016) built a tree-based machine learning classifier, using a set of features from these periodic candidates. Using the first LOTAAS data, Tan et al. (2018) next improved the feature selection, increased the training set size, and combined 5 decision trees into an ensemble classifier to further enhance the algorithm recall. Overall, these periodicity classifiers have helped discover many tens of new LOFAR pulsars.

The application of artificial intelligence (AI) to *single pulse* classification is less well developed, in part due to the nascency of FRB and rotating radio transient (RRAT) science. Though there is significant overlap with candidate ranking in pulsar periodicity searches, the problem of single-pulse classification has several distinctions, particularly for upcoming multi-beam real-time FRB surveys. These include the need for real-time classification for VOEvents and voltage dumps, as well as the usefulness of multi-beam information. Devine et al. (2016) developed a method for identifying clustered groups of dispersed pulses, primarily in order to discover pulsars that might be missed by periodicity searches. There, 16 group features (e.g., start-end DM, maximum signal-to-noise ratio S/N). are used in six traditional machine learning algorithms to find the best combination of hyperparameters and classifier. In

Arecibo’s commensal FRB search, ALFABURST, Foster et al. (2018) built a training set on 15,000 events and extracted 409 features from each. A random forest was then applied to group each trigger into one of nine classes. For the LOTAAS survey on LOFAR, Michilli (2018, accepted) adapted the Gaussian-Hellinger Very Fast Decision Tree used for periodicity classification (Lyon et al. 2016), and implemented a single-pulse search pipeline. It was trained on  $3.5 \times 10^4$  labelled RFI instances and  $1.8 \times 10^4$  thousand single pulses from 47 known pulsars as recorded in the LOTAAS data, and has discovered 7 pulsars based on features like pulse width, DM, and S/N vs. DM (Michilli 2018, accepted).

A next step, and challenge, in wide-field FRB searching will be the ALERT<sup>1</sup> survey on Apertif. An hierarchical series of beamforming starts with 39 compound beams (cf. Fig. 9) formed on each of the phased array feeds in the 12 dishes equipped with these. Every compound beam is next coherently beam-formed in 12 offset grating response beams; a refinement step of on-the-fly beam-forming, for removing chromatic sidelobe effects within this wide-bandwidth system, finally increase the beam count by a factor 6 for a total of  $\sim 2800$  synthesised beams (Maan & van Leeuwen 2017). These are searched in a real-time single-pulse pipeline powered by a large Graphical Processing Unit (GPU) cluster (ARTS; van Leeuwen et al. 2018). The ALERT survey will run 24/7 for approximately 3 calendar years. At  $2 \times$  the number of beams,  $5 \times$  the bandwidth, and more than  $10 \times$  the on-sky time of LOTAAS, the number of single-pulse

<sup>1</sup> [www.alert.eu](http://www.alert.eu)

candidates produced in ALERT is expected to not be humanly manageable.

In this paper we apply deep learning to the problem of single-pulse classification, for the first time. We develop a flexible toolkit that allows for the construction of hierarchical deep neural networks with multiple data products as inputs. Our approach will be useful both for multi-beam surveys as well as single-pixel telescopes. Classification can be done very quickly on GPUs by using the highly optimized software library, TensorFlow, which will be necessary if post-dedispersion real-time decisions are to be made. The paper is organized as follows: In Sec. 2 we introduce the key concepts of deep learning, and discuss its advantages of more traditional machine learning algorithms. In Sec. 3 we describe our model’s tree-like architecture, and show how arbitrary data inputs and feature extraction branches can be added to the network. We also offer tools to remedy the black box problem. Sec. 4 discusses how we assemble a labelled training set, despite there being only two dozen FRBs to-date. We then present the classifier’s results in Sec. 5, showing that very high recall and accuracy can be achieved with a sufficiently comprehensive training set. Sec. 6 asks if it would be possible to replace real-time dedispersion backends with a neural network classifier. We show that, somewhat surprisingly, forward-propagation through a simple convolutional neural network could be faster than brute-force dedispersion. However, simpler statistical approaches, like current dedispersion algorithms will always be more optimal, so such AI-based real-time classification may only be useful once unsupervised deep learning is more developed as a field.

## 2. DEEP LEARNING

Within the concentric circles of artificial intelligence (AI), machine learning has made the most progress in recent decades. Machine learning refers to a class of tools that aims to let computers learn without being explicitly programmed. Representation learning is a further subset of machine learning whose goal is not only to model the mapping from input features to output, but to actually discover the feature (or representation) itself (Goodfellow et al. 2016). Representation learning circumvents the limitations of “feature engineering”, in which data-specific features must be chosen by hand. This often requires domain expertise and can be time consuming. With real world data, extracting the salient features from input data tends to be difficult. The last subset in these concentric circles, deep learning, helps with the representation problem by building complexity

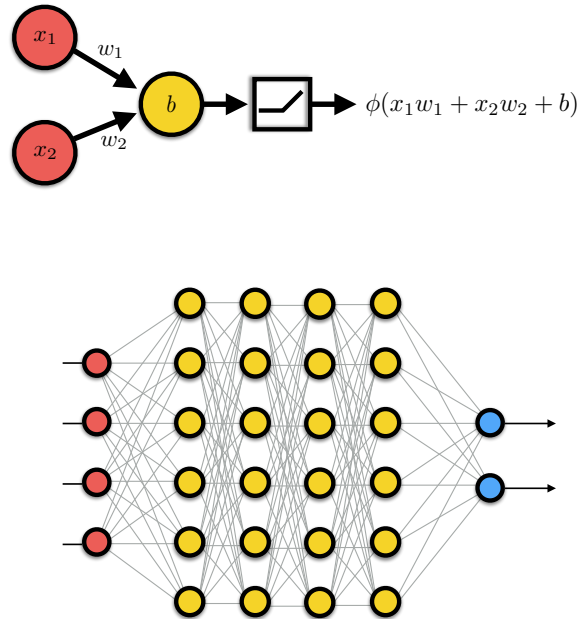


**Figure 2.** A schematic diagram of a perceptron (top), and a collection of perceptrons combined to form a neural network (bottom). The yellow nodes are artificial neurons, the red are input data, and the blue are output classes. The perceptron’s output is a non-linear function of the input vector,  $\mathbf{x}$ , projected onto the weight vector,  $\mathbf{w}$ , with some offset  $b$ . The network shown is a “deep neural network” because it has multiple hidden layers.

out of multiple, smaller, representations (Lecun et al. 2015; Goodfellow et al. 2016).

A deep neural network (DNN) is typically just a neural network that has multiple hidden layers. DNNs make use of the “multilayer perceptron”, a combination of artificial neurons and connections between them. Each subsequent hidden layers represents higher levels of abstraction of the input. A cartoon example of such a network is shown in Fig. 2. The perceptron has weights  $\mathbf{w} = (w_1, \dots, w_n)$  corresponding to each of the  $n$  connections with between the input data,  $\mathbf{x}$ , and a neuron, as well as a single offset value,  $b$ .

The perceptron computes a linear combination of the input with the weights, such that

$$z = \mathbf{x} \cdot \mathbf{w} + b. \quad (1)$$

A non-linear activation function is then applied to  $z$ , such that the output of the perceptron is some function  $\phi(z)$ . Such activators must be non-linear; otherwise, no matter how many hidden layers are in a network, the output would simply be a linear function of the input. It is also a problem that a linear activator’s gradient is independent of the input, making training via gradi-

ent descent impossible. Common examples include the logistic function,

$$\phi(z) = \frac{1}{1 + e^{-z}}, \quad (2)$$

a hyperbolic tangent,

$$\phi(z) = \tanh(z), \quad (3)$$

or a rectified linear unit (ReLU),

$$\phi(z) = \begin{cases} z & \text{for } z \geq 0 \\ 0 & \text{for } z \leq 0. \end{cases} \quad (4)$$

In this work we mostly use ReLU functions, which have been empirically found to be highly effective (Maas et al. 2013).

It is easy to see how complex functions could, in principle, be modelled by finding the right weight and offset parameters for each connection and neuron, given enough labelled input data. What is less obvious is why this can be done with relatively few parameters. The size of the input space of a  $100 \times 100$  greyscale image is  $256^{10000}$ , yet in many cases the mapping from input image to output class can be well approximated by  $\sim$  millions of parameters (Lin et al. 2017).

Irrespective of *why* deep learning has been so successful, its advancement of AI in recent years is undeniable. Deep learning has led to quantum leaps in self-driving car AI, super-human image recognition, natural language processing, and machine translation (Lecun et al. 2015; Goldberg 2015; Goodfellow et al. 2016).

One type of network, the convolutional neural network (CNN), has proven particularly powerful. Such architectures use convolution along with pooling to extract high-level features from input data. In the case of image recognition, an input image is typically convolved with multiple different kernels, which are meant to find structure in the data and identify relevant attributes. A non-linear activation function is then applied to the multiple convolved images, or “feature maps”. Each convolution step is followed by a “pooling” layer. The pooling can be as simple as taking the maximum pixel value in a small region (max pooling), and is meant to act as a summary statistic, allowing for some translation invariance and robustness against noise (Goodfellow et al. 2016). An example of our CNN is shown in Fig 3 with the real activations of an input dynamic spectrum generated by a trained model.

### 3. MULTI-INPUT CNN

The classification of dedispersed single-pulse candidates is slightly different from other problems to which

CNNs have been applied. For example, training a model for image recognition of, say, different breeds of dogs, requires building a network that can learn a very large and complex image space based on photos with effectively infinite S/N per pixel. FRBs occupy a much smaller volume of image space, but S/N per pixel is  $\sim 1$ . This turns out to be considerably less difficult than some other applications. Therefore we can achieve high recall and precision with modest-sized training sets (tens of thousands of triggers) and relatively few layers.

#### 3.1. Frequency-time data

The most informative input data array is the frequency-time intensity data, or dynamic spectrum. This input lends itself well to a 2D CNN, where image topology is preserved. In other machine learning algorithms such as support vector machines, 2D input data are flattened into a 1D vector. Dedispersion algorithms search a frequency-collapsed time series, triggering on outliers in one dimension. Therefore, at a single DM, valuable spectral information is thrown out where most false positives from thermal noise will not look like a broad-band pulse. By applying a deep CNN to the dynamic spectrum image the model can discriminate based on frequency structure.

Our dynamic spectrum model is a CNN with two convolutional layers, two max-pooling layers, and two fully connected layers. We pre-process input data by demanding that each trigger have unit variance and zero median. We find that input frequency-time arrays of shape  $32 \times 64$  allow for sufficient signal per pixel, but there is flexibility in the resolution of the input image.

A scaled-down example of this architecture is shown in Fig 3. The figure allows not only for visualization of the network’s architecture, but also a way of peeking inside the model and looking at each hidden layer’s activations. By saving the trained network’s weights and convolutional kernels, a given input array can be forward-propagated through the model to produce activations at each layer. The activations give one an idea of what the neural network “sees” in a given hidden layer, which alleviates the black box problem of DNNs, and is also helpful as a debugging tool. The CNN clearly tries to separate the input data’s background noise from the features intrinsic to the FRB pulse, such as a scattering tail.

#### 3.2. DM-time data

The DM-transformed data is a DM-time array whose rows are the frequency-collapsed time stream at a given DM. Broad-band, dispersed pulses will show up as a small island of preferred DM-time pairs, exhibiting a

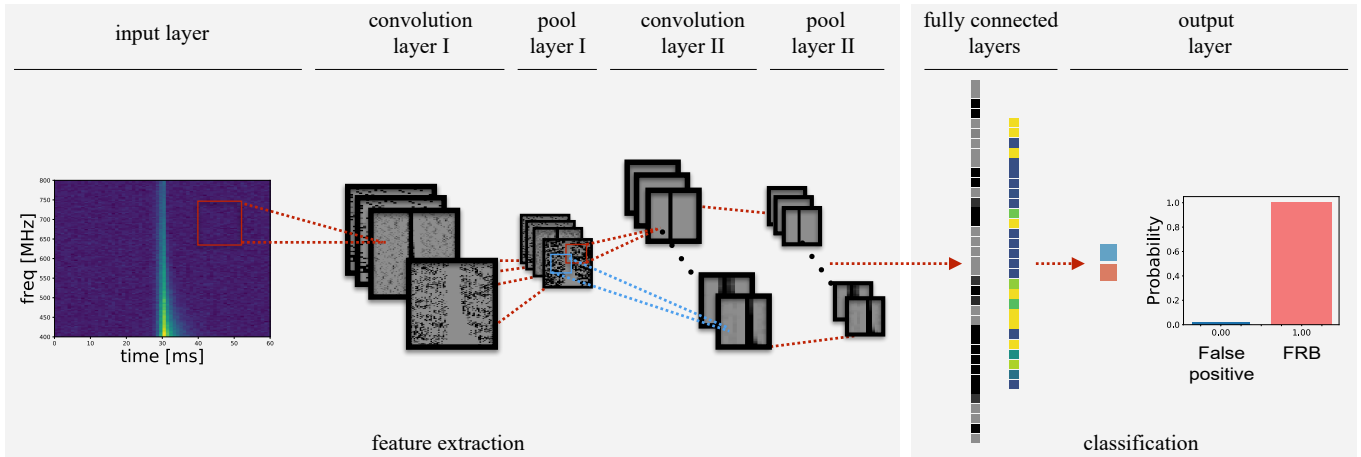


**Figure 3.** An example of our CNN architecture for the frequency-time array of a dedispersed FRB. The input image is a simulated strong, scattered burst, artificially bright for the sake of this example. The input data are convolved with 32 different convolutional kernels, the results of which are fed through a non-linear ReLu function, then reduced in a max pooling layer. 64 more kernels are then applied to the binned arrays, and pooling is done again by taking the maximum value in each  $2 \times 2$  bin. Each successive layer in the network’s feature extraction component is meant to discover features at higher levels of abstraction. We have included in this figure the real actualizations of a trained model for this input image. These give an idea of what the neural network’s classification is based on, and can help with the ‘black-box’ problem. After the fully connected layers, a probability is assigned to the trigger’s likelihood of being an FRB.

bow-tie pattern due to a degeneracy between optimal dispersion measure and pulse arrival time. For this input we also use a simple 2D CNN, with DM-time arrays of dimension  $100 \times 64$ . An example is shown in the third row from the top of Fig. 4

### 3.3. Pulse profile

We apply a one-dimensional CNN to the pulse profile dedispersed to the DM that maximizes S/N. The DNN’s first convolutional layer applies 32 length-5 kernels with strides of 2. After a 1d-max-pooling, another convolutional layer is applied with 64 length-2 kernels. The output is flattened and applied to a fully-connected layer with 1024 neurons.

### 3.4. Multi-beam detections

Most upcoming competitive FRB surveys will search multiple beams simultaneously. Objects beyond an antenna’s far-field limit are not expected to be seen in more than a couple of adjacent beams, whereas terrestrial RFI can be detected in many non-neighbouring beams. Other groups have taken this into account by rejecting triggers that showed up in unexpected beam permutations.

We allow our model to learn such permutations without explicitly telling it a given telescope’s on-sky beam configuration. This was done using a simple feed-forward neural network whose input data is a 1D length- $N_{\text{beam}}$  vector of detected S/N per beam. If no event was

found above the cutoff significance, a S/N of zero is assigned. After training, the model learns which beams ought not to trigger simultaneously, and which combinations are acceptable for a real astronomical detection.

### 3.5. DNN tree

We developed a multi-input neural network, to which arbitrary additional nets can be appended. The idea is to extract features from each input data product independently, since a given burst’s salient characteristics will depend on the space in which it is being viewed. The multiple networks can then be concatenated at the classification layers (in our case fully connected layers after convolution), creating a hierarchical tree-like neural network, shown in Fig. 4.

The first three data products we use in Fig. 4 are not independent. Indeed, their information content is highly redundant: The 1D pulse-profile is simply the dedispersed frequency-time array collapsed along the frequency axis; and the DM-time array is the frequency-time data after the DM transform. And yet empirically, better results are achieved by including combinations of the three than any individual one. This is because the feature extraction step is imperfect, so projecting the data in different ways allows the networks to detect different modes. The same is true for human classifiers. When sifting through pulse candidates one often looks at multiple statistics and figures with overlapping information.

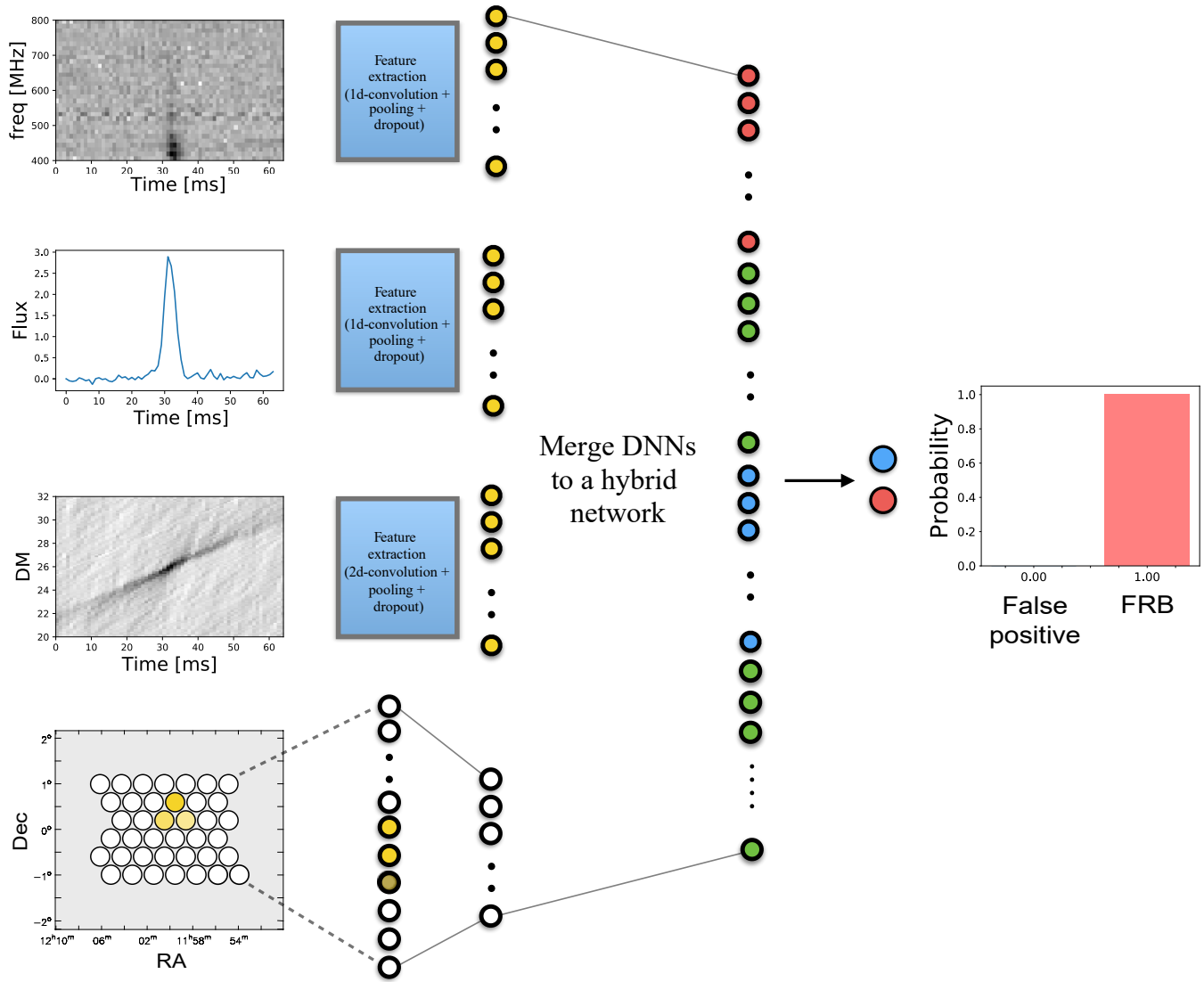


**Figure 4.** A hierarchical hybrid neural network built from concatenating multiple nets after their feature extraction layers, creating a large fully-connected layer resulting in a single binary classification for all inputs. Here we use as inputs the dedispersed frequency-time intensity array, the frequency-collapsed pulse profile, DM-time array, and multi-beam detection S/N, but our framework allows for any combination of these as well as additional input data products and networks. Since the full, merged DNN is trained together, the model will learn the relative importance of each input—for example, the dedispersed intensity array will tend to have more predictive power than the multi-beam statistics, thus the former will to have a greater influence on the output probability.

#### 4. TRAINING DATA

The two conditions that have allowed deep learning to thrive in this decade have been the availability of large, labelled data sets, and computers that can train multi-layer models in a reasonable amount of time. Despite the high all-sky event rate of FRBs, only a couple of dozen events have been discovered to-date (Petroff et al.

2016<sup>2</sup>). This presents a problem that does not exist for pulsar candidate classification. The small catalogue of real events is probably not yet a representative sample of the underlying burst population, nor is it big enough to build a meaningful training set for machine learning, deep or otherwise.

<sup>2</sup> <http://www.frbcat.org>

This means bursts can either be simulated, or single pulses from Galactic pulsars could be used as an approximation, or a combination of both. In this work we choose to simulate most of our “true-positives” and use false-positives that have been generated in real surveys and labelled by eye. We do not use single pulses from Galactic pulsars as a primary training set for the following reasons: Even though a large number of pulses can be collected from individual pulsars, the variation within FRBs (cf. the ASKAP set; [Bannister 2018, in prep](#)) appears to be larger than the pulse-to-pulse variation from a single pulsar, in terms of pulse characteristics (width, scattering, frequency structure, etc.). The differences between FRBs could also be larger than the variation between Galactic pulsars, given the extreme conditions they appear to live in ([Masui et al. 2015; Michilli et al. 2018](#)). FRB 121102 shows frequency structure on at least two different scales, and has bursts ranging in duration from  $30 \mu\text{s}$  to several ms ([Michilli et al. 2018](#)). Therefore, while a considerable training set could be built up from Galactic sources, the resulting model might be over-fit to the properties of the pulsars whose single pulses are bright enough to detect. Finally, while de-dispersed FRBs are qualitatively similar to single pulses from nearby pulsars ( $\sim$  millisecond-duration, broad-band, etc.), there may be systematic differences that are not obvious or visible, but that would bias the learner. In a simulated set there is more control and insight into the parameters producing the set that we train against.

While we choose to simulate our true-positives, false-positive triggers should not be simulated. Events generated by RFI, thermal noise, or dropped packets, occupy a much large volume of image space than single-pulses from FRBs, RRATs, or pulsars. Simulating RFI triggers would be difficult since there is no good model that describes such events. On top of that, each instrument will produce a different set of false-positives due to their disparate RFI environments and signal-processing back-ends. Conversely, single-pulses from FRBs can be modelled with far fewer parameters. Though they can suffer to varying degrees from temporal scattering, frequency scintillation, and DM-smearing, these effects can, in principle, be accounted for. By including a large collection of events that plausibly samples the full phase space of fast radio bursts in one’s training set, a sufficiently sized neural network can learn to identify a wide range of pulses. Casting such a wide net should catch true single-pulses.

We have built a training set from the 1268 hours of data in the CHIME Pathfinder incoherent-beam FRB search, plus simulated events injected into those data

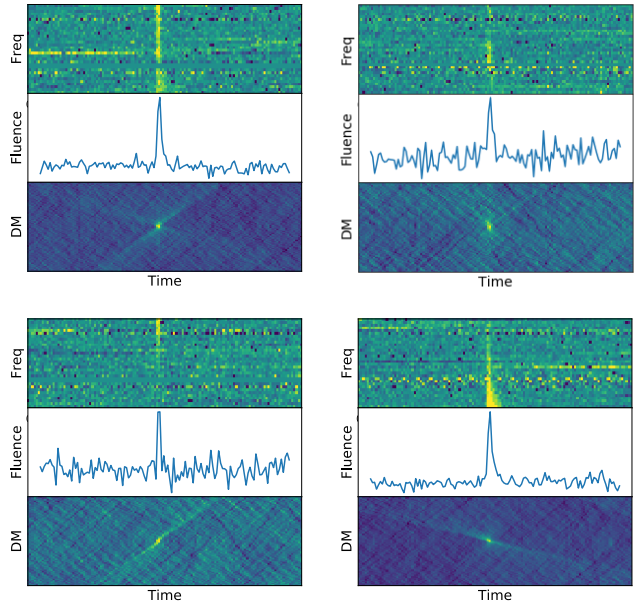


**Figure 5.** Four examples of simulated FRBs injected into real data. By combining thousands of these true-positives with known false-positives, we have built a large labelled training set. The three panels in each sub-figure are the frequency-time intensity array of the dedispersed pulse, the frequency-averaged pulse profile, and the DM-time intensity array (top to bottom). Combinations of these data products can be used as inputs to the multi-input neural net described in Sec. 3.

([Amiri et al. 2017](#)). We use 4650 events that triggered the dedispersion pipeline with a  $S/N$  above 10, but were found to be false-positives after inspection by eye. We then inject an equal number of simulated FRBs drawn from the distributions described in Sec. 4.1. Single pulses from known Galactic pulsars also triggered the search pipeline, including Crab giant pulses and individual pulses from PSR B0329+54. These astronomical true-positives were separated and used later in the verification of our model. For our Apertif model, the training set consists of 21246 candidates, half of which are known false positives. Of the remaining triggers, roughly 9800 are simulated FRBs added to real data, along with a couple of hundred single pulses from Galactic pulsars.

#### 4.1. Simulation

We simulate FRBs in one of three ways. The preferred approach is to randomly inject events in the data using the real-time tree dedispersion pipeline `burst_search`<sup>3</sup>. Another way is to add simulated FRBs to real background data that has already been dedispersed to a ran-

<sup>3</sup> [https://github.com/kiyo-masui/burst\\_search](https://github.com/kiyo-masui/burst_search)



dom DM. Finally, we can add pre-dedispersed FRBs to gaussian noise.

We calculate the pulse profile at each frequency by convolving a gaussian with a scattering profile,

$$s(t) = \frac{1}{\tau_\nu} e^{-t/\tau_\nu} \quad (5)$$

where  $\tau_\nu$  is the scattering timescale at a frequency  $\nu$  and is given by,

$$\tau_\nu = \tau_0 \left( \frac{\nu}{\nu_{\text{ref}}} \right)^{-4}, \quad (6)$$

for a reference frequency  $\nu_{\text{ref}}$ . The gaussian is taken to have width  $t_I$ ,

$$t_I^2 = t_i^2 + t_{\text{samp}}^2 + t_{\text{DM}}^2 \quad (7)$$

where  $t_i$  is the intrinsic pulse width,  $t_{\text{samp}}$  is the sampling time, and  $t_{\text{DM}}$  is the DM-smearing timescale.

Burst fluence is drawn from a Euclidean distribution, resulting in a S/N distribution of pulses that is also approximately Euclidean. Pulse widths are assumed to follow a log-normal distribution with mean 1.6 ms, resulting in widths between 0.1–50 ms. Scattering measure is log-uniform, in a way that roughly one in five bursts is noticeably temporarily scattered. Frequency scintillation is included via intensity modulation across the band using the positive half of a sinusoid with random phase and random decorrelation bandwidth. The scintillation bandwidth distribution is such that only about one third of simulated bursts show discernible frequency variation, consistent with the current population of detected FRBs. We take a uniform distribution of spectral index,  $\gamma$ , between  $-4$  and  $+4$ , where  $F_\nu \propto \nu^\gamma$ .

After signals are injected, events are kept if their S/N falls between 8–80. Ultra-bright events are discarded because they do not add much predictive power to the trained model; if a  $500\sigma$  event is found in the data, a model that has learned  $80\sigma$  events will still find it. All data are preprocessed to have unit variance and zero median. Uniformity in the treatment of both the simulated FRBs and the detected false-positives is important, because otherwise the binary classifier will learn based on trivial differences like noise RMS or power offset. In Fig. 5 we show examples of FRBs generated. The exact parameters of the distributions chosen are, of course, tunable, and will be subject to change depending on the survey for which the model is being built. The simulation tools are available on github<sup>4</sup>.

<sup>4</sup> [https://github.com/liamconnor/single\\_pulse\\_ml](https://github.com/liamconnor/single_pulse_ml)

## 4.2. RFI excision vs. classification

RFI will be an appreciable problem for all upcoming FRB surveys. Though we may want to mitigate RFI as much as possible, there exists a trade off between pre-dedispersion RFI cleaning and false positive rejection post-triggering. If one wants to minimize the number of RFI events triggered by a dedispersion algorithm, then data preprocessing needs to be done thoroughly. However, this runs the risk of over-cleaning the data and removing astronomical events. For example, if one of the steps in the RFI excision pipeline is a standard sigma-cut in which samples above, say,  $3\sigma$  in their local neighborhood are removed, then events like the Lorimer burst (Lorimer et al. 2007) or FRB 150807 (Ravi et al. 2016) could be missed, especially if the events fluctuate in frequency and time. Another approach would be to preserve as many triggers as possible by doing modest or no RFI cleaning, allow large numbers of false positives to trigger the dedispersion pipeline, and to only make a final decision after the triggers have been classified by the machine learning algorithm. This would make sense if one had high confidence in one’s classifier, otherwise real signals might drown in the flood of false positives. The solution is probably somewhere in between the two extremes: Data ought to be cleaned enough that the RFI within a time-frequency block containing an FRB does not decrease the event’s S/N. And a balance must be struck between the number of triggers generated and the risk of missed events, i.e. false negatives, which will require experimentation and will be survey-dependent.

## 5. RESULTS

In order to assess our model’s performance, we use standard metrics based on the confusion matrix. “accuracy” corresponds to the fraction of classified events that were labelled correctly, “precision” is the ratio of true positives to the number of events classified as positives, and “recall” is the fraction of true events that were labelled as such. Using TP, TN, FP, and FN as the number of true positives, true negatives, false positives, and false negatives respectively, the metrics are given by,

$$\text{acc} = \frac{\text{TP} + \text{TN}}{\text{TP} + \text{TN} + \text{FP} + \text{FN}} \quad (8)$$

$$\text{precision} = \frac{\text{TP}}{\text{TP} + \text{FP}} \quad (9)$$

$$\text{recall} = \frac{\text{TP}}{\text{TP} + \text{FN}}. \quad (10)$$

We care about the recall rate, because this determines the probability of missing an FRB. However, the precision is also important in case of real-time triggering.

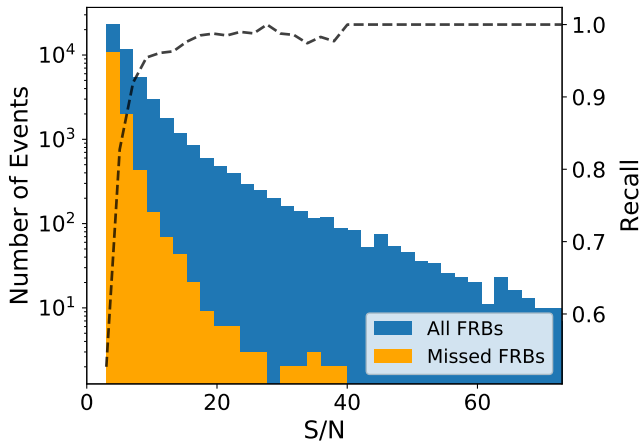


**Figure 6.** Statistics of missed FRBs as a function of signal to noise. The histogram shows the distribution of 50,000 simulated FRBs in the test set (blue) as well as the events from that test set that were mislabelled as RFI by our frequency-time 2D CNN (orange). The false-negative rate goes to 0.5 for low S/N, as expected, since a binary classifier with no predictive power will classify correctly half of the time. The fraction of recovered events, or recall, gets close to 1 for high S/N.

If voltage data are to be written after the dedispersion pipeline is triggered, as with ASKAP or UTMOST, then one must be sure that most of those events really are FRBs. The same is true for email notifications, VOEvents (Petroff et al. 2017), such as when Apertif will trigger LOFAR’s transient buffer boards for low-frequency localization.

In Fig. 6 we plot recall as a function of S/N. As expected, at very low S/N the model loses its predictive power: Recall drops to 50% because the algorithm is making a random guess at binary classification. However, above  $\sim 8\sigma$  the fraction of missed FRBs is quite flat, and also low, with recall and accuracy above 99%.

### 5.1. Cross-validation with pulsars

One must be cautious when including simulated events in a machine learning training set. For this reason we carried out tests in which classifiers trained on simulated FRBs were used to predict the labels of real single pulses from Galactic pulsars. We did this for both Apertif and CHIME Pathfinder data independently, using their respective hand-labelled false positives in combination with simulated bursts to train their DNNs. The models were then used on separate datasets containing hundreds of Crab giant pulses and B0329+54 single pulses. In Fig. 7 we show the output of our pipeline for the CHIME Pathfinder dataset. For the CHIME Pathfinder, a recall of  $\sim 99\%$  can be achieved. Our Apertif model was trained on  $\sim 20,000$  candidates and applied to several

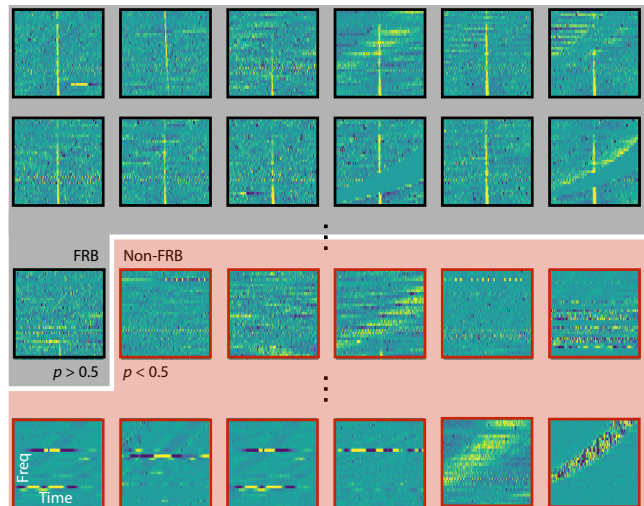


**Figure 7.** The ability of a model trained on simulated bursts to correctly identify Galactic pulsars. Our DNN classifier’s output is a list of triggers ranked by their probability of being an FRB. Shown are frequency (ordinate) versus time (abscissa) arrays of the test triggers, identical to the top panels in Fig. 5. The set includes real pulsars. Events that the classifier thinks are FRBs ( $p > 0.5$ ) are boxed in black, and non-FRBs are boxed in red. The most likely events are the top two rows, the marginal events are in the middle row, where the predicted labels transition from ‘FRB’ to ‘RFI’, and the final row are the least likely to be a true-positive. In this case we trained on 4850 known false positives from the CHIME Pathfinder, and 4850 simulated FRBs. The test data is a separate set of several hundred triggers consisting of known false positives, single pulses from B0329+54, and giant pulses from the Crab. The Pathfinder classifier gets fewer than 1% wrong. Our classifier trained on Apertif data achieves 99.7% recall.

hundred Galactic single pulses. It was able to recover 99.7% of these events.

### 5.2. Speed

For a given processor, training is always slower than classification since evaluation only requires one forward propagation through the neural network. For the applications described in previous sections, neither is prohibitively slow, even on CPUs. This is due to the modest sizes of the neural networks we have used (described in Sec. 3). However, for real-time FRB surveys like Apertif, ASKAP, UTMOST, and CHIME, it may be necessary to ‘decide’ on triggers quickly and without human inspection, for example if voltages are to be saved, or if an alert is to be sent to another telescope. Therefore, low-latency classification will be required. Our measurements of executions times for training and classification, shown in Fig. 7, indicate both can easily be done in real time on either CPUs and GPUs. A single GTX Titan X can classify 10<sup>4</sup> candidates in under a second. For

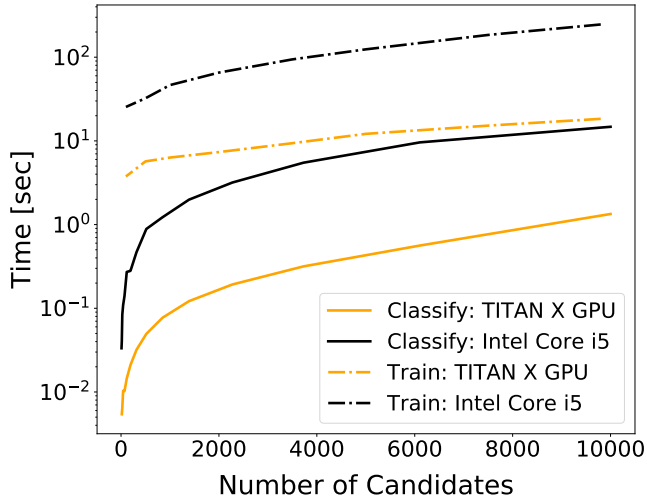


**Figure 8.** Classification and training time as a function of the number of dynamic spectra candidates. On a GTX Titan X GPU, classification takes  $\sim 100 \mu\text{s}$  per frequency-time array, using the network architecture described in Sec. 3 with the TensorFlow backend of keras. On a 2.9 GHz Intel Core i5-5287U CPU the classification time is a few milliseconds per candidate.

Apertif, the ARTS cluster contains 164 GTX 1080 Ti GPUs, which are each about twice as fast. Each Apertif compound beam (Fig. 9) is reduced on a dedicated 4-GPU server. The dedispersion and detection routines (AMBER<sup>5</sup>; Sclocco et al. 2016) require the usage of only 2 of these. After RFI mitigation, the trigger levels in the single-pulse S/N can be set in AMBER. Allowing of order 10 candidates to be marked as interesting, per second and per compound beam, would amount to  $>10$  million candidates per day; among which may be of order a single FRB. Even this liberal false-positive strategy could be easily further classified by the hybrid network, running on a single GPU on the central ARTS server and VOEvent issuer.

### 5.3. Phased array feed simulation

To test the efficacy of including multi-beam detection information in our DNN, we simulated the on-sky response within the 39 compound beams in the Apertif phased array feed (Fig. 9). We randomly scattered 10,000 FRBs within this multi-beam setup, currently planned for the imaging and time-domain surveys with Apertif<sup>6</sup>.

Events were drawn from a Euclidean flux distribution, and “detections” greater than  $6\sigma$  were recorded. Though the fraction of multi-beam detections depends

<sup>5</sup> <https://github.com/AA-ALERT/AMBER>

<sup>6</sup> <http://www.astron.nl/radio-observatory/apertif-surveys>



**Figure 9.** Lay out of the 39 compound beams that can maximally be formed at full bandwidth. This pattern provides the most uniform sensitivity over the celestial sphere possible (K. Hess, *priv. comm.*).

on the FRB brightness distribution, we found no significant differences when reasonable non-Euclidean values were used. RFI was assumed to show up in a random number of beams ranging from 1 to 39, following a log-normal distribution such that 75% of events are in detected in 5 or more beams. The training set was then taken to be 15,000 simulated length-39 S/N vectors. The feed-forward neural network is then tested on the remaining 5,000 events, with an accuracy of  $\sim 85\%$  and a slightly higher recall, when using the described configuration. This is much worse than the dynamic spectra CNN (accuracy above 99%), but that is to be expected. Seeing an event in only one beam does not preclude its being false positive, in the same way multi-beam detection does not guarantee that the event was RFI. The multi-beam data add orthogonal, complementary information to pulse shape and frequency structure, and was shown to be a valuable part of the hierarchical hybrid neural network (bottom row of Fig. 4).

## 6. REAL-TIME CLASSIFICATION WITH AI

Advances in signal processing allow the data volumes of future radio surveys to grow at considerable rates. As the same evolution will also generally permit hardware to keep up, parallelized versions of existing software tools may continue to analyze these data streams in real time (cf. Levin et al. 2017). But this data deluge will likely out-pace the ability of the end-user as-

tronomers to study all results. Interferometers like the Square Kilometer Array (SKA; Smits et al. 2009) and the next generation Very Large Array (ngVLA)<sup>7</sup> will not be able to search the newly available regions of parameter space simply by increasing power—new techniques must be developed. It is therefore reasonable to ask how advances in machine learning might aid this endeavour.

We investigate whether a real-time DNN classifier could be used for transient detection. For example, might it be possible to completely replace dedispersion backends with a pre-trained neural network? Even though the classifier could learn to identify arbitrary signals and not just  $\nu^{-2}$  sweeps, comparing to dedispersion provides a useful benchmark.

We can start by checking if any deep classifier could even keep up with the high data rates involved in real-time transient detection. The data rates on modern multi-pixel radio telescopes are enormous, meaning data must either be searched in real-time or binned down to lower resolution for offline processing. The scale of this challenge is exemplified by ARTS, the Apertif Radio Transient System (van Leeuwen 2014). Within each of the 39 compound beams (cf. Fig. 4), ARTS forms 12 tied-array beams for full sensitivity (Maan & van Leeuwen 2017), whenever the telescope is active. This continuously produces 225 Gbps of 300-MHz, 41  $\mu$ s data that needs to be searched in real-time. A massive dedicated cluster with 164 GPUs (GTX 1080 Ti) is required to keep up with this data rate.

In the case of real-time classification of FRBs, the idea would be to train on large numbers of dispersed pulses, such that the model would learn to look for  $\nu^{-2}$  sweeps, independent of their DM and with enough translational invariance to be insensitive to arrival times. This would supplant the need for dedispersion back-ends, which calculate a S/N after collapsing in frequency for multiple trial DMs.

In the past, offline processing and lower data rates meant brute-force dedispersion was sufficient. The brute-force algorithm requires summing  $N_f$  frequency channels for  $N_{DM}$  DM trials for all  $N_t$  time samples. Its computational complexity is  $\mathcal{O}(N_f N_t N_{DM})$  (Magro et al. 2011; Barsdell et al. 2012; Sclocco et al. 2014). Tree dedispersion applies a divide-and-conquer technique by taking advantage of the redundancy in dedispersion for nearby frequency channels (Taylor 1974). By using an FFT-like approach, the problem is reduced to a tree with  $\log_2 N_f$  branches, allowing for a  $\mathcal{O}(N_f N_t \log_2 N_f)$

complexity. A highly optimized CPU-based version of this algorithm has been implemented for CHIME’s FRB search (CHIME FRB Collaboration 2018, in prep). Other algorithms like the fast DM transform (FDMT) exploit the same redundancy and attempt to maintain optimality (Zackay & Ofek 2017). This algorithm is used in ASKAP’s FREDDA pipeline (Bannister 2018, in prep).

For a neural network like the one shown in Fig. 3, forward propagation is simply a series of convolutions and matrix multiplications. The two computational bottlenecks are the input layer, in which the  $N_f \times N_t$  array is convolved with  $n_{k_1}$  kernels, and the first fully-connected layer. A fully connected layer with  $n$  inputs and  $m$  outputs scales as  $\mathcal{O}(nm)$ . This is because the output is given by,

$$\mathbf{z} = \mathbf{W}\mathbf{x} + \mathbf{b} \quad (11)$$

where  $\mathbf{x}$  is the  $n$ -element input vector,  $\mathbf{b}$  is a vector containing offsets of the  $m$  neurons in that layer, and  $\mathbf{W}$  is an  $m \times n$  matrix whose elements  $w_{ij}$  give the connection between the  $j^{\text{th}}$  input and the  $i^{\text{th}}$  neuron.

In the final convolutional layer,  $n_{k_2}$  arrays are created, one for each kernel in the second convolution. The final pooling step takes these  $n_{k_2}$  matrices and reduces them in size by a factor of  $p_x p_y$ , by mapping each box of dimensions  $p_x$  by  $p_y$  to a single pixel in the subsequent layer. Therefore, the input of the first fully-connected layer is an unravelled vector of length

$$n_l = \frac{N_f N_t}{p_x^2 p_y^2} n_{k_2}, \quad (12)$$

since the original  $N_f \times N_t$  array has been reduced in size twice by a factor of  $p_x p_y$  through pooling. With  $n_{d_1}$  neurons in the first fully-connected layer, calculating the activations of this component scales as,

$$\mathcal{O}\left(\frac{N_f N_t}{p_x^2 p_y^2} n_{k_2} n_{d_1}\right). \quad (13)$$

This means if the network’s parameters are such that

$$\frac{n_{k_2} n_{d_1}}{p_x^2 p_y^2} < N_{DM} \quad (14)$$

then this layer can be computed faster than brute-force dedispersion. In the model we used for classification of already-dedispersed single pulses,  $p_x$  and  $p_y$  were both 2,  $n_{k_2} = 64$  kernels were used in the last convolutional layer, and the first fully-connected layer had  $n_{d_1} = 128$  neurons. Thus, the inequality in Eq. 14 would be satisfied for most brute-force searches, since the left side in our current model would be 512, whereas  $N_{DM} \sim 10^{3-4}$ .

<sup>7</sup> <http://ngvla.nrao.edu/>

For dedispersion algorithms that are more optimized, such as subband or tree dedispersion, the balance in Eq. 14 may be different; for tree dedispersion, the right-hand side term is  $\log_2 N_f$ , which is of order 10. So in contrast to the brute-force approach its computational intensity may be less than the DNN. That does not immediately imply, however, that the real-life performance of these optimized dispersion algorithms is proportionally faster. Dedispersion is a *memory* bound algorithm for real-world parameters. Through data reuse, brute force dedispersion can approach the execution time of the more optimized algorithms (Sclocco et al. 2016). Yet the fact that the matrix multiplications underlying the DNN are *compute* bound can give the classifier a further real-life advantage on compute-biased accelerators such as GPUs.

Forward propagation through the first layer of our CNN amounts to computing  $n_{k_1}$  convolutions. Convolution can be slow for two arrays of similar size. Using the brute-force method, this operation scales as  $\mathcal{O}(N^{2D})$ , where  $N$  is the input array’s length and  $D$  is number of dimensions. By invoking the convolution theorem, FFTs allow for a speed up, scaling as  $\mathcal{O}(N^D \log_2^D N)$ . However, our case is different from these, since our first layer requires convolving an  $N_f \times N_t$  array with a much smaller array, often with kernels of size  $3 \times 3$  or  $5 \times 5$ . The convolutions can be lowered to matrix multiplications, which are highly optimized on GPUs, allowing routines like `cuDNN` and `cuda-convnet2` high arithmetic intensity and efficiency (Chetlur et al. 2014). If we have a filter tensor that consists of  $n_{k_1}$  kernels of size  $n \times n$ , then that can be reshaped to an array of dimensions  $n_{k_1} \times n^2$ . With batches of  $N_b$  data arrays, and each of whose images are  $N_f \times N_t$ , then the data tensor can be reshaped to an  $n^2 \times N_b N_f N_t$  matrix. The convolution can then be computed as a matrix multiplication, which scales as,

$$\mathcal{O}(n_{k_1} n^2 N_b N_f N_t). \quad (15)$$

Therefore each frequency-time array takes on average  $n_{k_1} n^2 N_f N_t$  computations after dividing out the number of arrays per batch. In our case, with 16 or 32 length-3 square kernels, our most expensive convolutional layer is faster than brute-force dedispersion since  $n_{k_1} n^2 \approx 10^2 < N_{DM} \approx 10^4$ . There are further techniques that allow a large DNN to be approximated by a smaller one. The deeper and/or wider model would be trained offline, and its compactified version could be applied in real-time classification at a faster speed but with similar accuracy.

More than purely its speed, the sensitivity an algorithm provides is highly important when aiming to discover weak sources. Thus, despite the somewhat surprising fact that a moderate deep convolutional neu-

ral network could search raw intensity data faster than the brute-force dedispersion algorithm, we argue that dedispersion is not an ideal problem for deep learning. This is because algorithms like brute-force dedispersion, the FDMT, and tree-dedispersion are either optimal, or near-optimal in signal recovery. With a 2D CNN of only a dozen layers, the model is more successful if S/N does not fall significantly below  $\sim 1$  per pixel. The universal approximation theorem states that a finite feed-forward neural network can approximate arbitrary functions, meaning a sufficiently large network could, in principle, mimic optimal dedispersion (Cybenko 1989). However, the theorem says nothing about such a network being reasonably sized, nor about its learnability. Still, by demonstrating the low theoretical complexity of classification, the radio community can consider the problems for which real-time deep learning classifiers might be suited. In the following section we discuss this further.

## 7. DISCUSSION

In this work we have found it sufficient to simulate FRBs based on several parameters drawn from wide distributions. However if one wanted to improve the realism of true-positives in one’s training set, there are new techniques that can be employed. Generative adversarial networks (GANs) are a class of deep learning algorithms that could generate realistic FRB candidates. They consist of two adversarial networks: one that generates realizations, and another that attempts to discriminate real from simulated data (Goodfellow et al. 2014). The generator’s goal is to “fool” the discriminator, eventually resulting in a high error rate in classification. This has allowed for the creation of photo-realistic images based on drawings (Shrivastava et al. 2016). Guo et al. (2017) found that a standard deep CNN hit a performance ceiling for pulsar searching using real pulsars, so they used a deep convolutional GAN to build a collection of candidates. If such techniques were developed further, they may be useful for generating simulated RFI. In general, RFI is very difficult to model, but with an adversarial network trained on unlabelled real data, the problem of parametrizing it by hand could be overcome.

The black-box problem is another general concern about using deep neural networks in place of more explicit modelling. While we consider this a genuine issue for other problems, in the case of false-positive sifting our multi-input artificial net is no more opaque than a human scientist’s biological neural network. A human scientist knows some basic facts about dedispersed FRBs—they are roughly broad-band, narrow in time,

etc.—and then gets a “feel” for what false-positives look like by inspecting  $10^3$ – $10^4$  triggers. We never really know which features the expert has deemed salient, whereas in Fig. 3 we show the actual activations inside of our neural network for a given input. Therefore if our goal is simply to save time by accurately filtering out false-positives, the black-box problem is not a major consideration.

Having a machine learning classifier that can keep up with real-time triggers will be useful for a number of reasons. Even if all candidates are to be written to disk, the number of false positives may end up being prohibitively large for email notifications, outriggers, voltage dumps, or VOEvents. Because our neural network assigns a probability to each candidate, groups can set up a confidence threshold, below which triggers are saved but do not effect an alert.

We have also discussed the possibility of not only sifting through high-significance dedispersed candidates in real-time, but actually searching raw data in place of dedispersion backends. Beyond the optimized routines we described in Sec. 6, the training of, and classification with, deep neural nets is being made faster by tailored GPU hardware. Nvidia has released Tensor Cores in their Volta-based Tesla V100, which provide almost an order of magnitude speed up in matrix multiplication for large arrays over the Pascal-based P100 GPU. Google has also responded to the increased use of DNNs by building a custom application specific integrated circuit (ASIC) that they have called “Tensor Processing Units” (TPUs) (Jouppi et al. 2017). These TPUs cannot yet help train neural networks, but were built specifically for classification, ideal for what we have described in Sec. 6.

We showed that the computational complexity of a single forward propagation through a modest CNN can be significantly less than that of brute-force dedispersion. Furthermore, dedispersion algorithms tend to have low arithmetic intensity which means they are memory bound and not ideal for GPUs. Classification using neural networks amounts to a series of matrix multiplications, accelerated by previously discussed hardware. However, we argue that a CNN could not reach the level of statistical optimality of known dedispersion algorithms without making the network so large that gains in speed were lost.

Applying deep learning to real-time transient detection may still be useful in upcoming surveys. Dedispersion algorithms search for signals with  $\nu^{-2}$  sweeps, caused by the differential group velocity of light in cold dense plasmas. Deviations from such a quadratic dis-

persion relation can come from relativistic plasmas, or electrons whose plasma frequency is close to the observing frequency. Unusual polarization signatures can be induced by propagation, which can be searched for (Kennett & Melrose 1998). SETI might also find these techniques useful in searching for bright, structured signals from extraterrestrial civilizations. But history teaches us that the most exciting discoveries in transient astronomy come from “unknown unknowns”, usually by searching a parameter space that was not previously accessible. The SKA and ngVLA will offer such datasets, and their availability may coincide with great advances in unsupervised, or semi-supervised learning.

## 8. CONCLUSIONS

We have applied deep learning to the problem of single-pulse classification, with large real-time FRB surveys in mind. Using Google’s TensorFlow we developed a multi-input deep neural network that takes FRB candidate diagnostic data, such as dynamic spectra, the DM-time intensity array, and multi-beam information, and returns a probability of the event being real. Models can be trained offline but applied in real-time, allowing for low-latency classification if outriggers, VOEvents (Petroff et al. 2017), or voltage dumps are to be triggered. These tools are available on github<sup>8</sup>.

The possibility of replacing dedispersion backends with a single DNN classifier was investigated. Although statistical optimality to purely quadratically dispersed signals may not be achievable without cumbersome multi-layer models, we showed that forward propagation could be done more efficiently and quickly than brute-force dedispersion on modern hardware. Thus, deep learning classification of signals more diverse than dispersion is feasible, on raw data, in real-time.

We thank Emily Petroff for helpful comments on the manuscript. We thank the CHIME Collaboration for allowing the usage of data from its Pathfinder instrument, and the Apertif Survey Team for the use of the ARTS false-positive dataset. We also thank Jorn Peters, Yunfan (Gerry) Zhang, and Folkert Huizinga for useful discussions. The research leading to these results has received funding from the European Research Council under the European Union’s Seventh Framework Programme (FP/2007-2013) / ERC Grant Agreement n. 617199, and from the Netherlands Research School for Astronomy (NOVA4-ARTS).

<sup>8</sup> [https://github.com/liamconnor/single\\_pulse\\_ml](https://github.com/liamconnor/single_pulse_ml)

## REFERENCES

- Amiri, M., Bandura, K., Berger, P., et al. 2017, *ApJ*, **844**, 161
- Bannister. 2018, in prep, in prep
- Bannister, K. W., Shannon, R. M., Macquart, J.-P., et al. 2017, *ApJL*, **841**, L12
- Barsdell, B. R., Bailes, M., Barnes, D. G., & Fluke, C. J. 2012, *MNRAS*, **422**, 379
- Caleb, M., Flynn, C., Bailes, M., et al. 2017, *MNRAS*, **468**, 3746
- Chetlur, S., Woolley, C., Vandermersch, P., et al. 2014, ArXiv e-prints, [arXiv:1410.0759](https://arxiv.org/abs/1410.0759)
- CHIME FRB Collaboration. 2018, in prep, in prep
- Coenen, T., van Leeuwen, J., Hessels, J. W. T., et al. 2014, *A&A*, **570**, A60
- Cybenko, G. 1989, *Mathematics of control, signals and systems*, **2**, 303
- Devine, T. R., Goseva-Popstojanova, K., & McLaughlin, M. 2016, *MNRAS*, **459**, 1519
- Foster, G., Karastergiou, A., Golpayegani, G., et al. 2018, *MNRAS*, **474**, 3847
- Goldberg, Y. 2015, ArXiv e-prints, [arXiv:1510.00726](https://arxiv.org/abs/1510.00726) [cs.CL]
- Goodfellow, I., Bengio, Y., & Courville, A. 2016, *Deep Learning* (MIT Press), <http://www.deeplearningbook.org>
- Goodfellow, I. J., Pouget-Abadie, J., Mirza, M., et al. 2014, ArXiv e-prints, [arXiv:1406.2661](https://arxiv.org/abs/1406.2661) [stat.ML]
- Guo, P., Duan, F., Wang, P., Yao, Y., & Xin, X. 2017, ArXiv e-prints, [arXiv:1711.10339](https://arxiv.org/abs/1711.10339) [astro-ph.IM]
- Jouppi, N. P., Young, C., Patil, N., et al. 2017, ArXiv e-prints, [arXiv:1704.04760](https://arxiv.org/abs/1704.04760)
- Kennett, M., & Melrose, D. 1998, *PASA*, **15**, 211
- Lecun, Y., Bengio, Y., & Hinton, G. 2015, *Nature*, **521**, 436
- Levin, L., Armour, W., Baffa, C., et al. 2017, ArXiv e-prints, [arXiv:1712.01008](https://arxiv.org/abs/1712.01008) [astro-ph.IM]
- Lin, H. W., Tegmark, M., & Rolnick, D. 2017, *Journal of Statistical Physics*, **168**, 1223
- Lorimer, D. R., Bailes, M., McLaughlin, M. A., Narkevic, D. J., & Crawford, F. 2007, *Science*, **318**, 777
- Lyon, R. J., Stappers, B. W., Cooper, S., Brooke, J. M., & Knowles, J. D. 2016, *MNRAS*, **459**, [arXiv:1603.05166](https://arxiv.org/abs/1603.05166) [astro-ph.IM]
- Maan, Y., & van Leeuwen, J. 2017, ArXiv e-prints, [arXiv:1709.06104](https://arxiv.org/abs/1709.06104) [astro-ph.IM]
- Maas, A. L., Hannun, A. Y., & Ng, A. Y. 2013in
- Magro, A., Karastergiou, A., Salvini, S., et al. 2011, *MNRAS*, **417**, 2642
- Marcote, B., Paragi, Z., Hessels, J. W. T., et al. 2017, *ApJL*, **834**, L8
- Masui, K., Lin, H.-H., Sievers, J., et al. 2015, *Nature*, **528**, 523
- Michilli. 2018, accepted, *MNRAS*
- Michilli, D., Seymour, A., Hessels, J. W. T., et al. 2018, *Nature*, **553**, 182
- Ng, C., Vanderlinde, K., Paradise, A., et al. 2017, ArXiv e-prints, [arXiv:1702.04728](https://arxiv.org/abs/1702.04728) [astro-ph.IM]
- Petroff, E., Bailes, M., Barr, E. D., et al. 2015, *MNRAS*, **447**, 246
- Petroff, E., Barr, E. D., Jameson, A., et al. 2016, *PASA*, **33**, e045
- Petroff, E., Houben, L., Bannister, K., et al. 2017, ArXiv e-prints, [arXiv:1710.08155](https://arxiv.org/abs/1710.08155) [astro-ph.IM]
- Ravi, V., Shannon, R. M., Bailes, M., et al. 2016, *Science*, **354**, 1249
- Rosen, R., Swiggum, J., McLaughlin, M. A., et al. 2013, *ApJ*, **768**, 85
- Scholz, P., Spitler, L. G., Hessels, J. W. T., et al. 2016, *ApJ*, **833**, 177
- Sclocco, A., van Leeuwen, J., Bal, H. E., & van Nieuwpoort, R. V. 2016, *Astronomy and Computing*, **14**, 1
- Sclocco, A., Van Nieuwpoort, R., & Bal, H. E. 2014, in *Exascale Radio Astronomy*, Vol. 2
- Shrivastava, A., Pfister, T., Tuzel, O., et al. 2016, ArXiv e-prints, [arXiv:1612.07828](https://arxiv.org/abs/1612.07828) [cs.CV]
- Smits, R., Kramer, M., Stappers, B., et al. 2009, *A&A*, **493**, 1161
- Spitler, L. G., Cordes, J. M., Hessels, J. W. T., et al. 2014, *ApJ*, **790**, 101
- Spitler, L. G., Scholz, P., Hessels, J. W. T., et al. 2016, *Nature*, **531**, 202
- Straal, S., & van Leeuwen, J. 2018, *A&A*, in prep
- Tan, C. M., Lyon, R. J., Stappers, B. W., et al. 2018, *MNRAS*, **474**, 4571
- Taylor, J. H. 1974, *A&AS*, **15**, 367
- Tendulkar, S. P., Bassa, C. G., Cordes, J. M., et al. 2017, *ApJL*, **834**, L7
- Thornton, D., Stappers, B., Bailes, M., et al. 2013, *Science*, **341**, 53
- van Leeuwen, J. 2014, in *The Third Hot-wiring the Transient Universe Workshop*, ed. P. R. Wozniak, M. J. Graham, A. A. Mahabal, & R. Seaman, 79
- van Leeuwen, J., Kooistra, E., Connor, L., et al. 2018, in prep
- van Leeuwen, J., & Stappers, B. W. 2010, *A&A*, **509**, 7
- Zackay, B., & Ofek, E. O. 2017, *ApJ*, **835**, 11
- Zhu, W. W., Berndsen, A., Madsen, E. C., et al. 2014, *ApJ*, **781**, 117